Crustal Structures and Anisotropy in Southeastern China: Continental Collision and Intraplate Earthquakes

H. B. Huang[1], E. Y. He[1], H. Jiang[1,2], J. Guo[1,2] and X. L. Qiu[1,2]

[1] South China Sea Institute of Oceanology, CAS, Guangzhou, P.R. China.

[2] University of Chinese Academy of Sciences, Beijing, P.R. China

Corresponding author: Haibo Huang (go223@scsio.ac.cn)

Key Points:

- Crustal structures reveal the differential evolution between continental blocks
- Stratified anisotropy inherited from foliation and shearing due to past subduction.
- Present collision reactivates the fault and seismicity along the block boundaries.

Abstract

This study investigates the role of crustal structures and anisotropy in southeastern China in the context of intraplate earthquakes resulting from concentrated and perturbed tectonic stresses. The region is characterized by a complex multiphase tectonic history and undergoing collision between the Philippine Plate and the South China Margin. Using the teleseismic receiver function method, we provide a detailed picture of crustal structures and layered anisotropy in Guangdong and Fujian, two earthquake-prone regions. The results show that the crustal anisotropy is stratified into two layers, with the upper-middle crust having an orogen-perpendicular slow axis and the lower crust with a fast axis aligned with the orogen. The lateral heterogeneity and anisotropy of the crustal structure highlight the boundary and differential movement between the continental blocks. The increase in density and intensity of intraplate earthquakes across this boundary supports our conclusion of a link between decoupled crustal deformation and seismicity. Specifically, foliation of the metamorphic rocks during the Mesozoic collision generated the orogen-parallel fabrics in the upper-middle crust, ductile shearing yielded orogen-perpendicular fast directions at the lower crust, and mismatch evolution between continental blocks reactivated by present collision provides stress conditions conducive to the occurrence of earthquakes in southeastern China. Our findings provide insights into the mechanism of intraplate earthquakes and the tectonic evolution of continental collision zones.

Plain Language Summary

How intraplate earthquakes happen is a topic of interest in the study of continental collision at plate margins. We investigate the role of crustal structures and anisotropy in southeastern China in the context of these earthquakes. This region, undergoing collision between the Philippine Plate and the South China Margin, has a multiphase tectonic history including

remnants of paleo-Pacific subduction. Using the receiver function method, we provide a detailed picture of crustal structures and layered anisotropy in Guangdong and Fujian, two earthquake-prone regions in southeastern China. The results show that anisotropy in the crust is stratified into two layers: an upper-middle crust with an orogen-perpendicular slow axis, and a lower crust with a fast axis aligned with the orogen. The lateral heterogeneity and anisotropy of the crustal structure highlight the boundary and differential movement between the continental blocks. The increase in density and intensity of intraplate earthquakes across this boundary supports a link between decoupled crustal deformation and seismicity, in which (1) metamorphic foliation in the upper-middle crust was caused by the Mesozoic collision (2) the lower crust characterizes ductile shearing, and (3) mismatch evolution between continental blocks reactivated by present collision provides stress conditions conducive to the occurrence of earthquakes.

1 Introduction

Intraplate earthquakes have been recorded in stable continental interiors, oceanic plates, and continental collision zones. The mechanisms underlying intraplate earthquakes are generally related to the presence of preexisting faults or fractures in the Earth's crust, which can be reactivated by ongoing geologic processes (Vilotte et al., 1982; Gray and Pysklywec, 2012). The relationship between intraplate earthquakes and continental collision is a subject of ongoing research, and there are still many unanswered questions about the precise mechanisms that lead to seismic activity in these regions. However, recent studies have shed light on some of the key factors involved, including the role of crustal structures and anisotropy. For example, using the shear-wave splitting method, a study by Meltzer et al. (2007) found that the crustal anisotropy in southeastern Tibet is related to the ongoing collision between the Indian Plate and the Eurasian Plate. Similarly, a study by Duan et al. (2022) found that the 2019 Ridgecrest earthquakes in

California were related to preexisting faults in the Earth's crust that were reactivated by the ongoing tectonic stresses associated with the collision between the Pacific Plate and the North American Plate. Therefore, continental collisions result in concentrated and perturbed tectonic stresses in the crust, and how these stresses evolved has important implications for understanding the Earth's tectonic processes and the effects on intraplate earthquakes.

Seismic anisotropy, which refers to the variation in seismic velocity in different directions, can provide insight into the lithospheric deformation and stress state in collided continents (Godfrey et al., 2002). Anisotropy in the brittle crust is often associated with the presence of cracks and can reflect the direction of current regional stress (Bianchi et al., 2015; Levin and Park, 1998). For example, when the maximum compressive is perpendicular to the crack plane, it closes the cracks and causes the seismic waves to travel faster in that direction. In the middle and lower crust, under high confining pressures, the formation of anisotropy is dominated by the preferential alignment of minerals and strain-related crystal orientation (Fry et al., 2010). As a result, regions that have been subjected to intense tectonic activity tend to show fast anisotropy along the strike of geological terranes. However, local tectonic processes such as active faults or magmatic intrusions can affect the background anisotropy and reveal structural heterogeneity (Audet, 2015; Boness and Zoback, 2006).

In this study, we investigated the crustal thickness and Poisson's ratio in Southeastern China (SC) using teleseismic receiver functions (RFs) recorded by permanent stations in Fujian and Guangdong Provinces (Figure. 1). These areas experienced multiphased continental collisions between various plates since the Mesozoic, and the intraplate earthaquakes are also noticeable and have been the focus of the research (Hsu et al., 2004; Zhu et al., 2020). We employed harmonic decomposition and waveform inversion of the RFs to determine the depth

variable anisotropy and dipping layer in the crust of the SC and to explore the connection between the crustal deformation and the imprinted tectogenesis. Additionally, we analyzed the potential impact of the tectonically active Bashi Fault Zone (BFZ) on crustal anisotropy and the mechanism for triggering the intraplate earthquakes in the region.

2 Geological Settings

The SC lies at the junction of a passive South China Sea continental margin and an active orogenic belt across Taiwan (Figure. 1). Collision and subduction in the paleo-Tethyan and Pacific tectonic domains have contributed to the geologic structures of the SC (Li et al., 2019; Suo et al., 2019). The collage of distant paleocontinents with various basement ages was completed after the subduction between the paleo Pacific and Eurasian Plates in the Mesozoic (Hsu et al., 1988; Zhou and Li, 2000). As a result, the region is characterized by extensive tectonic mélange zones and nappe structures that run roughly SE-EW (Li et al., 2020). As an overlay of multiple collision processes, how the orogeny constructed and modified the geological structures in time and space has been a global concern. Particularly, in which way the lithospheric materials were deformed and redistributed provides insights into the dynamics and mass circulation of the Plate motion system.

The collision between the Philippine Sea plate and the South China Sea continental plate is causing significant crustal deformation in the SC. The collision is occurring in the northwest direction at a speed of ~82 mm/yr (Huang et al., 2015b). However, GPS studies have shown that the vertical motion of the crust in the SC coastal area is far less compared to the east coast mountains of Taiwan (Hu et al., 2001; Liu et al., 2007; Yu et al., 1997). This means that most of the stress generated by the collision is absorbed in the thrust front. Despite this, nonnegligible compressive stresses have been transported to the SC by a series of NW trending faults such as

the BFZ (Ding and Liang, 1992). These transverse structures interact with the NE trending faults in the SC and are increasing the risk that strong and intense earthquakes in the conjunction zones (Hsu et al., 2004). Especially, southern Fujian and eastern Guangdong, where the BFZ extends, experience the highest frequency of earthquakes with magnitudes above M6.0. There have even been repeated earthquakes with magnitudes greater than M7.0, which are rare in the entire SC region (Zhu et al., 2020). However, the extent and mechanism of these earthquakes are not well understood, as the impact of the multiple collisions on the current deformation and stress state of the lithosphere is not well known.

3 Methods and Results

3.1 Data Processing and RF Computation

Since the groundbreaking work of Langston (1979) and Owens et al. (1984), the RF has been established as an effective technique for isolating the structural responses beneath the seismic station (Ammon, 1991; Ball et al., 2014; Huang et al., 2015a). The method, which unitizes the P-to-S converted waves (Ps) generated when a propagating P wave encounters a velocity boundary along its path, enables high-vertical-resolution imaging of crustal and mantle discontinuities. For isotropic structures, the RF method can be used to estimate crustal thickness and *Vp/Vs* ratio by stacking amplitudes at predicted Ps and multiple reflection times from different epicenters and directions (*H-k* stacking) (Zhu and Kanamori, 2000). For anisotropic structures, systematic variations in amplitudes, polarity, and travel times of the radial and transverse components of the RF along the ray paths are observed due to azimuth-dependent anisotropy (Levin and Park, 1998). Based on these observations, the RF modeling will provide

131 constraints on the depth and degree of the anisotropy structures on horizontal scales of several
132 kilometers in the crust.

133 This study analyzed data from 126 permanent seismic stations run by the China
134 Earthquake Administration between 2009 and 2015. Teleseismic waveform recordings with a
135 magnitude greater than M6.0 and epicentral distances ranging from 30° to 90° were considered.
136 The back azimuth coverage of these events is overall adequate for anisotropy analysis (Figure.2).
137 The RFs were computed following the source equalization procedure with a water-level
138 parameter of 0.001 and a Gaussian width of 2.5 (Ammon, 1991). We manually evaluated these
139 receiver functions by checking the Ps signals, and a total of 24874 pairs of radial and transverse
140 RFs were selected for further processing. For anisotropy modeling, the RFs were moveout
141 corrected at a slowness of 0.06 s/km and stacked into 10° back azimuths.

142 ### 3.2 Anisotropy Analysis and Harmonic Decomposition

143 The investigation of crustal anisotropy was mainly based on the variation in the
144 waveform of the radial and transverse RFs with azimuth. The moveout-corrected RFs were
145 plotted as a function of back azimuth and showed significant amplitudes and periodic variations
146 on the transverse and radial RFs (Figure.2a). On the radial RFs, the Ps phase from the Moho was
147 observed to arrive at approximately 3.5s and exhibit a periodic variation of 180° with azimuth
148 (Figure.2a), which is indicative of anisotropy in the crust. In addition, polarity reversals were
149 often observed at the zero-lag time on the transverse RFs with a period of 360°, indicating the
150 presence of a dipping boundary in the shallow layer (Frederiksen and Bostock, 2000; Tsang-Hin-
151 Sun et al., 2021). The presence of additional reversed polarity sequences prior to the arrival of
152 the Ps phase further confirmed the existence of anisotropy layers with plunging axes or dipping
153 interfaces in the crust (Figure.2b).

To analyze the periodic characteristics of various sources, we employed harmonic decomposition in the study of inclined boundaries and anisotropy (Audet, 2015; Bianchi et al., 2015; Shiomi and Park, 2008). This technique represents the RF ensemble as a combination of $\cos(k\varphi)$ and $\sin(k\varphi)$, where k is the harmonic degree and φ is the back azimuth (Supporting Information). The degree-0 harmonic (A) represents the contribution from flat-layered isotropic media and can be used to determine the velocity structures unaffected by azimuthal heterogeneity. The degree-1 harmonics (*B1, B2*) indicate a dipping boundary or anisotropy with a plunging axis, while the degree-2 ones (*C1, C2*) denote anisotropy with a horizontal axis. Based on Audet (2015), we constructed the decomposition system and solved the matrix to identify the direction in which a particular harmonic component is optimized. We choose to minimize the variance of *B2*, and the optimized azimuth can be interpreted as the tilt direction of the isotropic layer, or it can be directly related to the trend of the anisotropy axis. In accordance with Audet (2015), we used the time range of 0 ~ 7.0 s to obtain stable harmonics originating from both dipping boundaries and crustal anisotropy. Additionally, we examined the time window from -1.0 s to 1.0 s to find the signals from shallow dipping layers.

Figure.3 illustrates the five scaling factors for the harmonic degrees 0, 1, and 2 at stations NPDK and YND. Both stations display positive amplitudes for isotropic component A at around 3.5 s, indicating the presence of P-to-S converted phases from the Moho boundary. In addition, many stations show negative amplitudes before the Moho phases, indicating a potential low-velocity layer, as reported in previous studies (Huang et al., 2020; Zhou et al., 2020). Component *B1* is characterized by alternating positive and negative pulses, with the strongest pulse appearing at the start and suggesting the presence of a dipping boundary at the top. A second set of double-polarity phases can be seen between about 2 and 3 s, which could be due to depth-

177 dependent crustal anisotropy or dipping layers. This is further supported by the signals in *B2*, as
178 a uniform azimuth model may not fully account for layered anisotropic axes. We have compared
179 the spatial characteristics of the anisotropy by drawing the harmonic profiles across different
180 regions (Figure. 4). The similarity between the degree-1 and degree-2 profiles would suggest a
181 gentle plunge of the anisotropy axis.

182 3.3 Synthetic Modeling and Anisotropy Uncertanty

183 The optimization of variance in multiple time windows for the backazimuthal harmonics
184 may not accurately separate the depth-variable anisotropy (Supporting Information, Figure.1S-
185 7S). Instead, we resort to synthetic modeling and nonlinear inversion of the binned RFs using the
186 method proposed by Frederiksen and Bostock (2000) and Frederiksen et al. (2003). The synthetic
187 modeling and inversion of the RFs use the techniques of efficient forward-modeling of the RFs
188 and a directed Monte Carlo search of the model space guided by the neighbourhood algorithm
189 (Frederiksen et al., 2003; Sambridge, 1999). The model that best synthesizes the weighted radial
190 and transverse RF pairs is found by generating a number N of random points in the model space,
191 dividing the remaining space into neighborhoods closest to one sampled point using the L2-norm
192 distance metric, and selecting a number M of points in the neighborhoods with low misfit to the
193 real RF data for further search. The model space is iterated by repeating the search steps.

194 The initial model was parameterized into three layers based on geological information
195 and harmonic analysis: weathered granite and volcanic layer, and two anisotropy layers with
196 slow and fast axes. The slow axis was found to well represent the minerals and cracks in the
197 upper crust while the fast axis better approximated mineral alignment or rock fabric in the lower
198 crust (Cossette et al., 2016). The upper mantle was assumed to be constant during the inversion.
199 First, the thicknesses of the weathered granite layer and the dipping angle and strike were

searched, using an averaged crustal thickness and seismic velocity, with weight coefficients for the radial and transverse RFs set to be 0.1 and 0.9, respectively. The dipping strike can generally be determined by the polarity reversal of the signals around zero time. After determining the inclined layer, the thickness and anisotropy of the two crustal layers were searched through 60 iterations using sample sizes N of 30 models and retention samples M of 10 models. Forward modeling was then performed to simplify the structures and modify the anomalous results that overfit the data. If necessary, the misfit was reduced further by adding a layer to the crustal model obtained from inversion. The inverted model parameters can be found in the Supporting Information (Table 2S). The strikes of the inclined layer of the top layer and the anisotropy axes were not always consistent between the harmonic analysis and waveform modeling (Table.2S). However, the anisotropy axes obtained from the harmonic analysis are generally consistent with the inversion results in azimuth (Figure.2c) but show a more dispersed distribution, possibly due to the influence of the inclined interface or separation failure of layered anisotropy. Figure.5 shows the RF modeling from stations of GD_XNH with two anisotropic layers and FJ_HAHF with single anisotropic layer, and both stations have shallow dipping layers on top of the models.

To understand the contribution of the accepted model to the RFs, each inverted model parameter was used to generate theoretical RF waveforms (Figure.6). While the monolayer model was acceptable at some stations (Figure.5a), the bilayer model could better reproduce the pulses on the two components in most cases (Figure.5b and Figure.6). As shown in Figure.6, the results indicate that the inclined weathered granite layer generates polarity reversal around 0 s, while the layered anisotropy contributes to the signals from 1 to 4 s, especially in the transverse RF. With the addition of the fast anisotropy layer, the positive signals at around 1.8 s in the radial and transverse RFs were better fitted. In the following discussion, we focus on the

223 directions among the model parameters, as the orientation of the anisotropy axes and the strike of
224 the dipping layer are more robust (Bianchi et al., 2015). The results are summarized in Figure.2c,
225 including the strike of the dipping layer and the orientation of the slow and fast axis. In which,
226 the strikes of the dipping layers have a concentrated distribution with an average value of 225°.
227 The azimuth of the slow and fast axes had two peaks at 140° and 225°, with the former being the
228 dominant one.

229 ### 3.4 Crustal Thickness and *Vp/Vs* Ratio Estimation

230 Crustal thickness and *Vp/Vs* ratio beneath each station were estimated by applying the *H-*
231 *k* method to the unsorted RFs. For stations with missing available data, we referred to the results
232 from Huang et al. (2015a) obtained using recordings from 2001 to 2008. We used the same
233 stacking parameters to make sure that the results are comparable. The updated map of the
234 thickness and *Vp/Vs* ratio is similar to the previous results, but it provides more detailed evidence
235 of block partitioning and corresponding petrological differences (Figure.7). Combined with the
236 spatial characteristics of the relocated seismicity (Lu et al., 2022), the map shows two subzones
237 roughly belonging to Fujian and Guangdong respectively with a boundary consistent with the
238 BFZ in location and strike. The *Vp/Vs* value shows a scattered anomaly greater than 1.9 along
239 this boundary, but it is normal on both sides and increases slightly toward the sea and reaches the
240 minimum value in Guangdong (Figure.7b). Overall, the mean *Vp/Vs* value across the whole
241 region is 1.76, but it shows a higher value (~1.77) in the northeast of the BFZ than the southwest
242 (~1.74). The crustal thickness has an overall mean value of ~29.5 km and shows obvious zoning
243 characteristics, in which Fujian has a mean value of ~31 km, about 2 km higher than Guangdong
244 and its adjacent area (~29km). The region with thickened crust was bounded by the BFZ in the

northeast and the Changle-Nanao fault zone (CNFZ) in the northwest, forming a sharp junction zone at Nanao Island (Figure.7a).

4 Discussion

4.1 Crustal Structure and Tectonic Boundaries Between Collided Blocks in the SC

The tectonic evolution of the South China (SC) region is governed by the rheological properties and deformation mechanisms of the continental crust, which have been investigated using various methods such as stratigraphy, petrology, and geophysical surveys (Kang et al., 2006; Li et al., 2020; Li et al., 2019). However, there is still a lack of evidence from deep structures in this area. Our study reveals a significant difference in the crustal thickness between Guangdong and Fujian Province (Figure.7a), with Fujian's crust being approximately ~3 km thicker than that of Guangdong and Taiwan Strait, separated by the BFZ and the CNFZ. While the *Vp/Vs* ratio of Fujian slightly increases towards the sea, the entire region displays a relatively low value of around 1.73 (Figure.7b). The precision of the crustal thickness in the Taiwan Strait is limited by the availability of offshore stations. However, joint modeling of artificial seismic data and free-air gravity anomalies confirms the difference in crustal thickness across the CNFZ (Wang et al., 2017). The SC has experienced collisional orogeny and crustal thickening since the Mesozoic, with modification by volcanism. The slightly increased crustal thickness and low *Vp/Vs* ratio in Fujian may suggest that the felsic upper crust has accreted to a greater extent (Huang et al., 2014; Huang et al., 2020), consistent with the presence of widespread low-velocity layers and negative RF pulses beneath the upper crust (Zhou et al., 2020), which could act as a napping interface for the upper crust.

Lithospheric extension during the Late Mesozoic and Cenozoic periods played a significant role in shaping the collisional blocks and likely led to the opening of the South China Sea. Many Cenozoic basins are located primarily in the southeastern part of the SC, and previous research has confirmed the existence of a rifting center in Guangdong (Huang et al., 2020; Lu et al., 2022). The relatively thin crust in this region is consistent with the continental extension. The decrease in the *Vp/Vs* ratio at the same time would draw the assumption that the mafic middle-to-lower crust may have flowed or been stretched more significantly (Ji et al., 2009). Isotopic characteristics of the granite in SC indicate limited contamination of the mantle material in its formation. The upwelling mantle only transferred the heat into the crust, causing the melting of felsic rocks in the middle-to-lower crust, which may further maintain a low *Vp/Vs* ratio (Huang et al., 2020).

The distinct crustal structures and rock composition properties result in different deforming mechanisms between the continental blocks of Guangdong and Fujian. GPS-based leveling measurements show that crustal deformation within the contacting zone along the BFZ is intensive, where the crustal movement has the most significant differential activity (Liu et al., 1998). The offset of the Moho across the BFZ may indicate the assembly of microcontinents in the SC. Tomography studies have also found that prominent low-velocity areas can extend throughout the entire crust along this boundary, and it may act as a conduit for the upwelling mantle materials (Cao et al., 2022; Li et al., 2014). According to this study, the area with a high *Vp/Vs* ratio along this boundary may have been affected by the fracturing and volcanism during the continental collision and shearing along the BFZ.

4.2 The Interplay between Inherited and Current Orogeny

Our study reveals a depth-dependent anisotropy in the crust, with the upper layer exhibiting slow anisotropy that is roughly parallel to the fast one in the lower layer (Figure.7). This bilayer anisotropy, which varies in type and orientation, may reflect the decouple crustal deformation and unique sources of the anisotropy. We propose that the presence of strain fabric and cracks in the crust are the two main factors behind the observed crustal anisotropy. If cracks were responsible for the anisotropy in the upper crust, the current axis of the maximum compressive stress (NW-oriented) would result in a slow axis in the NE direction, which contradicts the observations made through GPS and the focal mechanism (Levin and Park, 1998; Yang et al., 2011). Furthermore, the first layer's depth (5-15 km) may be too deep for cracks to remain open (Nakamura et al., 1996). An alternative explanation for the slow direction of the brittle crust is orogen-parallel anisotropy (OPA), which indicates strain-related anisotropy (Fry et al., 2014). Compression during collision causes foliation in metamorphic rocks and alignment of mica in the crust, leading to deformational fabrics that are parallel to the fold structures. The NEE-SWW orientation of the P-wave ellipsoid in the widely distributed Paleozoic S-type granitoids in Guangdong also suggests strong compression in the NNW-SSE direction (Jiang et al., 1995), which is in agreement with the field schistosity. The tilt direction of the dipping layer is also found to be similar to the strike of the slow anisotropy axis (Figure.7), indicating that the dipping layer formed during the same deformation process as the schistosity (Schulte-Pelkum and Mahan, 2014). The top low-velocity crustal layer is believed to represent weathered or eroded granite and volcanic bodies caused by uplifting due to compression. Local cracks or tectonics should not be excluded, as some studies using noise tomography and shear wave splitting of regional earthquakes have obtained scattered results (Wu et al., 2007).

The lower crustal anisotropy is typically interpreted as aligned anisotropy minerals resulting from ductile deformation and shear-induced crustal flow (Bianchi et al., 2015; Fry et al., 2014). The NW-oriented anisotropy axis in SC aligns with the widespread collision and the late lithospheric extension caused by the subduction between the paleo-Pacific Plates and the Eurasian Plate. The layered anisotropy structures like those observed in the SC have been observed in many other orogenic places (Fry et al., 2010; Huang et al., 2015b; Lu et al., 2014), and have been proposed to be present in the ongoing Taiwan orogeny (Huang et al., 2015b), which supports a common mechanism for crustal deformation during orogeny (Figure.8). The widely distributed low-velocity layer in the lower crust of SC could be considered a remnant shearing zone that accommodates the layered deformation of the upper and lower crust (Huang et al., 2020; Li et al., 2020).

4.3 Significance for Intracontinental Earthquake Analysis

In Southeastern China, recent and historical earthquakes are distributed along the NE-trending fault zones, which intersect with the NW-trending BFZ (Ding and Liang, 1992; Zhu et al., 2020). The contrasting structures of the crustal thickness and *Vp/Vs* ratio suggest that the Fujian and Guangdong provinces have distinct properties in lithospheric strength. Among the transverse structures spanning the SC and Taiwan strait, the crustal deformation in the south is more intense and complex due to the compression between the SC and the Philippine Sea plate (Shen et al., 2009). As Fujian is located at the front of the Taiwan orogenic belt, the napping of the upper crust makes it more brittle and likely to deform (Fry et al., 2010). GPS measurements also show that the Fujian area is bounded by two high-strain crustal deformation belts in the SW and NE edges, with non-uniform horizontal velocity within the region (Liu et al., 1998). This results in inconsistent azimuths of the anisotropy axis in Fujian (Figure.7 and Figure.8),

particularly along the BFZ in both the upper and lower crusts. Across the BFZ, the axis azimuth rotated from NW to NNE, and the dipping direction also shows variation. The above-mentioned anomaly suggests a mismatch in block evolution separated by the BFZ, leading to the potential for pervasive strain accumulation along the boundary.

The boundary is also a seismic gap zone, and the earthquake at the edge of the two regions is the most intensive in the whole area. Nanao Island has experienced repeated devastating earthquakes in conjunction with the BFZ and the littoral fault belt (Xia et al., 2020). In the plane view, crustal structures in this conjunction area are quite distinct in terms of crustal thickness, *Vp/Vs* ratio, and anisotropy. However, the precise location and focal mechanism of these earthquakes are unclear due to the lack of recorded seismic data (Kang et al., 2006). We propose that the decoupled crustal deformation and block boundary may provide proper conditions for stress concentration and release, thus allowing for dense seismicity. Anisotropy and structural changes can be used as indicators to assess the risk of large earthquakes, but the aftershock effect on the regional stress field and crustal deformation should be investigated in the future (Wang and Shen, 2020).

5 Conclusions

We utilized teleseismic receiver functions to examine the crustal structure and seismic anisotropy in the coastal region of southeast China. The results revealed a difference in the crustal thickness and *Vp/Vs* ratio between Guangdong and Fujian provinces, which are separated by the high-intensity earthquake zone along the NW-trending BFZ. The crust exhibits decoupled deformation processes, including thickening of the upper-middle crust due to paleo-Pacific subduction beneath the South China margin and flows in the lower crust in response to the lithospheric extension. The *Vp/Vs* ratio has a low-to-intermediate value throughout the region,

but shows a dispersed high value along the BFZ, indicating fracturing during the continental collision and stress transportation. Harmonic decomposition and modeling of the receiver function indicate layered anisotropy overlaid by a dipping weathered granite layer. The upper-middle crust has a slow-axis anisotropy parallel to the orogen, resulting from strain-related rock foliation due to subduction-induced thrusting. Below the upper-middle crust, a fast anisotropy is found and interpreted as aligned anisotropy minerals caused by ductile shearing and crustal flow. The anisotropy axis rotates from NW in Guangdong to NNE in Fujian across the BFZ, suggesting mismatch evolution between the two blocks. Pervasive strain accumulation and stress perturbation in the BFZ could be reactivated by the present collision of the Philippine Sea Plate onto the South China margin. The decoupled crustal deformation and mismatch evolution of the continental blocks could provide seismogenic conditions for intraplate earthquakes.

Acknowledgments

This study was supported by the Key Special Project for Introduced Talents Team of Southern Marine Science and Engineering Guangdong Laboratory (Guangzhou) [grant number: GML2019ZD0204], the National Science Foundation of China [grant numbers: 42176081], and the Youth Innovation Promotion Association CAS (2021344). The GMT software (Wessel and Smith, 1995) was used to plot the figures. We thank Pascal Audet for providing code packages for the harmonic decomposition of receiver functions, and A.W. Frederiksen for receiver function modeling code packages. We also thank Mikael Evain for his insightful comments.

Open Research

Seismic data for this study are provided by Guangdong Seismic Network, Guangdong Earthquake Agency, and the data can be found at the link http://doi.org/10.5281/zenodo.7794196.

References

Ammon, C.J., (1991). The Isolation of Receiver Effects from Teleseismic P-Wave-Forms. *Bulletin of the Seismological Society of America*, 81, 2504-2510.

Audet, P., (2015). Layered crustal anisotropy around the San Andreas Fault near Parkfield, California. *J Geophys Res-Sol Ea*, 120, 3527-3543.

Ball, J.S., Sheehan, A.F., Stachnik, J.C., Lin, F.C., Collins, J.A., (2014). A joint Monte Carlo analysis of seafloor compliance, Rayleigh wave dispersion and receiver functions at ocean bottom seismic stations offshore New Zealand. *Geochem Geophy Geosy*, 15, 5051-5068.

Bianchi, I., Bokelmann, G., Shiomi, K., (2015). Crustal anisotropy across northern Japan from receiver functions. *J Geophys Res-Sol Ea,* 120, 4998-5012.

Boness, N.L., Zoback, M.D., (2006). Mapping stress and structurally controlled crustal shear velocity anisotropy in California. *Geology*, 34, 825-828.

Cao, L.M., Yuan, H.Y., Zhao, L., Zhao, M.H., Huang, H.B., Hao, T.Y., Qiu, X.L., (2022). Fault-controlled regional magmatism and mineral deposition in central Cathaysia-Evidence from ambient noise tomography. *Sci China Earth Sci,* 65, 1715-1735.

Cossette, E., Audet, P., Schneider, D., Grasemann, B., (2016). Structure and anisotropy of the crust in the Cyclades, Greece, using receiver functions constrained by in situ rock textural data. *J Geophys Res-Sol Ea*, 121, 2661-2678.

399 Ding, Y.Z., Liang, L., (1992). Earthquake risk in the structure of Bashi system. South China
400 *Journal of Seismology*, 12, 1-13.
401 Duan, H.D., Chu, Z.M., Zhang, S.C., Yang, C.S., Chen, J.Y., Lei J.Z., (2022). Analysis of
402 coseismic slip distributions and stress variation of the 2019 Mw 6.4 and 7.1 earthquakes in
403 Rdigecrest, California. *Tectonophysics*, 831(20), doi: 10.1016/j.tecto.2022.229343.
404 Frederiksen, A.W., Bostock, M.G., (2000). Modelling teleseismic waves in dipping anisotropic
405 structures. *Geophysical Journal International*, 141, 401-412.
406 Frederiksen, A.W., Folsom, H., Zandt, G., (2003). Neighbourhood inversion of teleseismic Ps
407 conversions for anisotropy and layer dip. *Geophysical Journal International* ,155, 200-212.
408 Fry, B., Davey, F., Eberhart-Phillips, D., Lebedev, S., (2014). Depth variable crustal anisotropy,
409 patterns of crustal weakness, and destructive earthquakes in Canterbury, New Zealand. *Earth*
410 *Planet Sc Lett,* 392, 50-57.
411 Fry, B., Deschamps, F., Kissling, E., Stehly, L., Giardini, D., (2010). Layered azimuthal
412 anisotropy of Rayleigh wave phase velocities in the European Alpine lithosphere inferred from
413 ambient noise. *Earth Planet Sc Lett*, 297, 95-102.
414 Godfrey, N.J., Christensen, N.I., Okaya, D.A., (2002). The effect of crustal anisotropy on
415 reflector depth and velocity determination from wide-angle seismic data: a synthetic example
416 based on South Island, New Zealand. *Tectonophysics,* 355, 145-161.
417 Gray, R., Pysklywec, R.N., (2012). Geodynamic models of mature continental collision:
418 Evolution of an orogen from lithospheric subduction to continental retreat/delamination. *Journal*
419 *of Geophysical Research*, 117(B3), doi: 10.1029/2011JB008692.
420 Hsu, K.J., Sun, S., Li, J.L., Chen, H.H., Pen, H.P., Sengor, A.M.C., (1988). Mesozoic Overthrust
421 Tectonics in South China. *Geology,* 16, 418-421.

422 Hsu, S.K., Yeh, Y.C., Doo, W.B., Tsai, C.H., (2004). New bathymetry and magnetic lineations
423 identifications in the northernmost South China Sea and their tectonic implications. *Marine*
424 *Geophysical Research*, 25, 29-44.
425 Hu, J.C., Yu, S.B., Angelier, J., Chu, H.T., (2001). Active deformation of Taiwan from GPS
426 measurements and numerical simulations. *J Geophys Res-Sol Ea*, 106, 2265-2280.
427 Huang, H.B., Guo, X.W., Xia, S.H., Qiu, X.L., 2014. Study of crustal thickness and Poisson's
428 ratio in the coastal area of South China. Chinese J. Geophys. (in Chinese), 57(6), doi:
429 10.1002/cjg2.20148
430 Huang, H.B., Tosi, N., Chang, S.J., Xia, S.H., Qiu, X.L., (2015a). Receiver function imaging of
431 the mantle transition zone beneath the South China Block. *Geochem Geophy Geosy*, 16, 3666-
432 3678.
433 Huang, H.B., Xiong, H., Qiu, X.L., Li, Y.H., (2020). Crustal structure and magmatic evolution in
434 the Pearl River Delta of the Cathaysia Block: New constraints from receiver function modeling.
435 *Tectonophysics,* 778, doi: 10.1016/j.tecto.2020.228365.
436 Huang, T.Y., Gung, Y., Kuo, B.Y., Chiao, L.Y., Chen, Y.N., (2015b). Layered deformation in
437 the Taiwan orogen. *Science*, 349, 720-723.
438 Ji, S.C., Wang, Q., Salisbury, M.H., (2009). Composition and tectonic evolution of the Chinese
439 continental crust constrained by Poisson's ratio. *Tectonophysics*, 463, 15-30.
440 Jiang, J.S., Yang, S.F., Chen, H.L., Zhu, G.Q., Wang, Z.G., Ji, Z.L., Zhang, B.Y., Guo, S.J.,
441 (1995). The elastic properties of S-type and I-type granitoids in Guangdong Province and their
442 tectonic meaning. *Geological Journal of Universities,* 1, 34-40.
443 Kang, Y., Yang, X., Lu, J.S., Chen, X., Chen, G.M., (2006). Characteristics of focal mechanism
444 in Guangdong and its adjacent areas, *Earthquake Research in China,* 20, 19-36.

445 Langston, C.A., (1979). Structure under Mount Rainier, Washington, Inferred from Teleseismic
446 Body Waves. *J Geophys Res,* 84, 4749-4762.
447 Levin, V., Park, J., (1998). P-SH conversions in layered media with hexagonally symmetric
448 anisotropy: A cookbook. *Pure Appl Geophys*, 151, 669-697.
449 Li, J.H., Cawood, P.A., Ratschbacher, L., Zhang, Y.Q., Dong, S.W., Xin, Y.J., Yang, H., Zhang,
450 P.X., (2020). Building Southeast China in the late Mesozoic: Insights from alternating episodes
451 of shortening and extension along the Lianhuashan fault zone. *Earth-Sci Rev*, 201, doi:
452 10.1016/j.earscirev.2019.103056
453 Li, S.Z., Suo, Y.H., Li, X.Y., Zho, J., Santosh, M., Wang, P.C., Wang, G.Z., Guo, L.L., Yu, S.Y.,
454 Lan, H.Y., Dai, L.M., Zhou, Z.Z., Cao, X.Z., Zhu, J.J., Liu, B., Jiang, S.H., Wang, G., Zhang,
455 G.W., (2019). Mesozoic tectono-magmatic response in the East Asian ocean-continent
456 connection zone to subduction of the Paleo-Pacific Plate. *Earth-Sci Rev*, 192, 91-137.
457 Li, Z.N., Zheng, Y., Xiong, X., Lin, S., Chen, X.X., Bao, T., Chen, G., (2014). Research on
458 crustal three dimensional velocity structure in Fujian-Taiwan region and its tectonic implication.
459 *Journal of Seismological Research*, 37, 29-38.
460 Liu, X.Y., Guo, F.Y., Lin, J.H., Huan, S.M., (2007). The primary analysis on crust movement
461 and GPS survey results in Fujian inshor. *Fujian Seismology*, 15, 25-32.
462 Liu, Y.K., Guo, F.Y., Chen, Z.H., Huang, L.R., Ma, Q.R., (1998). Recent crustal vertical
463 movement and fault activity of Fujian Province. *Crustal Deformation and Earthquake*, 18, 68-
464 73.
465 Lu, G., Zhao, L., Zheng, T.Y., Kaus, B.J.P., (2014). Strong intracontinental lithospheric
466 deformation in South China: Implications from seismic observations and geodynamic modeling.
467 *J Asian Earth Sci,* 86, 106-116.

Lu, Z.Y., Huang, H.B., Ye, X.W., Lu, J.S., Xiong, C., (2022). High-Resolution Crustal Shear-Wave Velocity Structure in the Pearl River Delta, South China. *Seismol Res Lett,* 93, 338-350.

Meltzer, A., Burgmann, R., van der Hilst, R.D., et al., (2007). Geodynamics of the southeastern Tibetan Plateau from seismic anisotropy and geodesy. *Geology*, 35(6), 563-566.

Nakamura, M., Ando, M., Kusunose, K., Sato, T., (1996). Depth-dependent crustal anisotropy at midwestern Honshu, Japan. *Geophysical Research Letters,* 23, 3417-3420.

Owens, T.J., Zandt, G., Taylor, S.R., (1984). Seismic Evidence for an Ancient Rift beneath the Cumberland Plateau, Tennessee - a Detailed Analysis of Broad-Band Teleseismic P-Waveforms. *J Geophys Res*, 89, 7783-7795.

Schulte-Pelkum, V., Mahan, K.H., (2014). A method for mapping crustal deformation and anisotropy with receiver functions and first results from USArray. *Earth Planet Sc Lett*, 402, 221-233.

Shen, J.R., Xu, S.Y., Fu, W.J., (2009). Transverse structure of Taiwan Strait area and its effect on the earthquakes of southeast coastal regions. *Geotectonica et Metallogenia,* 32, 535-541.

Shiomi, K., Park, J., (2008). Structural features of the subducting slab beneath the Kii Peninsula, central Japan: Seismic evidence of slab segmentation, dehydration, and anisotropy. *J Geophys Res-Sol Ea,* 113, doi: 10.1029/2007JB005535.

Suo, Y.H., Li, S.Z., Jin, C., Zhang, Y., Zhou, J., Li, X.Y., Wang, P.C., Liu, Z., Wang, X.Y., Somerville, I., (2019). Eastward tectonic migration and transition of the Jurassic-Cretaceous Andean-type continental margin along Southeast China. *Earth-Sci Rev*, 196.

Tsang-Hin-Sun, E., Evain, M., Julia, J., Lamarque, G., Schnurle, P., (2021). Crustal seismic structure and anisotropy of Madagascar and southeastern Africa using receiver function

harmonics: interplay of inherited local heterogeneities and current regional stress. *Geophysical Journal International*, 226, 660-675.

Vilotte, J.P., Daignieres, M., Madariage, R., (1982). Numerical modeling of intraplate deformation: Simple mechanical models of continental collision. *Journal of Geophysical Research*, 87(B13): 10709-10728.

Wang, M., Shen, Z.K., (2020). Present-Day Crustal Deformation of Continental China Derived From GPS and Its Tectonic Implications. *J Geophys Res-Sol Ea,* 125, doi: 10.1029/2019JB018774

Wang, S., Qiu, X.L., Zhao, M.H., Yan, P., Chen, X.Z., Li, P.C., Fang, W.H., (2017). Imaging crustal structure variation across the Changle-Nan'ao fault zone by the joint inversion of seismic and gravity data. *Chinese J. Geophys. (in Chinese)*, 60, 3853-3862.

Wu, J., Gao, Y., Cai, J.A., Shi, Y.T., Lin, S., B.T., Li, Z.Y., (2007). Preliminary study on seismic anisotropy in the crust in southeast of Cathaysia Block. *Chinese J. Geophys. (in Chinese)*, 50, 1748-1756.

Xia, S.H., Zhou, P.X., Zhao, D.P., Cao, J.H., (2020). Seismogenic structure in the source zone of the 1918 M7.5 NanAo earthquake in the northern South China Sea. *Phys Earth Planet In*, 302, doi:10.1016/j.pepi.2020.106472

Yang, Z.H., Sheehan, A., Shearer, P., (2011). Stress-induced upper crustal anisotropy in southern California. *J Geophys Res-Sol Ea*, 116, doi: 10.1029/2010JB007655

Yu, S.B., Chen, H.Y., Kuo, L.C., (1997). Velocity field of GPS stations in the Taiwan area. *Tectonophysics,* 274, 41-59.

511 Zhou, P.X., Xia, S.H., Hetenyi, G., Monteiller, V., Chevrot, S., Sun, J., (2020). Seismic imaging
512 of a mid-crustal low-velocity layer beneath the northern coast of the South China Sea and its
513 tectonic implications. *Phys Earth Planet In*, 308, doi: 10.1016/j.pepi.2020.106573
514 Zhou, X.M., Li, W.X., (2000). Origin of Late Mesozoic igneous rocks in Southeastern China:
515 implications for lithosphere subduction and underplating of mafic magmas. *Tectonophysics,* 326,
516 269-287.
517 Zhu, J.J., Li, S.Z., Chen, X.L., Li, J., Li, Y., Xing, H.L., Jia, Y.G., (2020). Large intraplate
518 earthquakes and static stress changes in the South China coastal region. *Gondwana Res*,102,46-
519 59.
520 Zhu, L.P., Kanamori, H., (2000). Moho depth variation in southern California from teleseismic
521 receiver functions. *J Geophys Res-Sol Ea,* 105, 2969-2980.
522
523

Figure.1 Map of faults and seismicity in southeastern China. The red and black triangles represent the seismic stations with and without acceptable anisotropy results, respectively. The yellow dots indicate the earthquake epicenters as reported in (Lu et al., 2022). The solid lines represent the regional faults that were identified through field investigation and seismic exploration. The dashed lines with triangles mark the nappe belts formed by the collision between Taiwan and the Philippine Sea plate. The green dashed line represents the Changle-Nanao Fault Zone (CNFZ). BFZ: Bashi Fault zone. The inset map highlights the locations of teleseismic events, represented by red stars, and the earthquake station SHG is marked by a black triangle.

Figure.2 The radial (a) and tangential (b) receiver functions recorded at the station SHG. The red and blue colors represent positive and negative phases, respectively. The dashed line indicates the periodic variation of the Ps phases, which correspond to anisotropy. (c). The Rose diagram shows the azimuths of the slow axis (represented by gray), the fast axis (light blue), and the optimized angle obtained through harmonic decomposition (green). The strike of the dipping layer is depicted in orange. The radii of the vectors are proportional to the frequency of the corresponding value, and the sectors have a width of 8° in degrees.

Figure.3 Harmonic decomposition of receiver functions for stations NPDK in Fujian (a) and YND in Guangdong (b). Each harmonic component is represented by a vertical trace and labeled at the bottom. The time range in which the B2 was searched for the minimum value was from 0 to 7 s. The direct P wave and its primary converted phase Ps are marked on component A.

545 **Figure. 4** Results of harmonic decomposition showing the B1 (a, b) and B2 (c, d) of all the
546 stations. Station names and the corresponding optimized angle are indicated at the top and
547 bottom of the figures. Red and blue colors show positive and negative amplitudes.

548

549 **Figure.5** Two examples of the synthetic modeling of the binned RFs from the station FJ_HAHF
550 (a) in Fujian and GD_XNH (b) in Guangdong. The solid lines indicate the theoretical RFs, while
551 the color-shaded curves are observed RFs. The anisotropy structures can be found in Supporting
552 Information (Table. S2).

553

554 **Figure. 6** Reliability test of the synthetic modeling of the RFs for GD_XNH. The top and bottom
555 rows show the radial and transverse components, respectively. The blue boxes indicate the
556 contribution of each model parameter to the RFs. The model parameters can be found in
557 Supporting Information (Table.S1 and Table. S2).

558

559 **Figure.7** Maps of the inverted dipping direction shown in red arrows, the trend of the slow
560 anisotropy axis shown in gray bars, and the fast axis in white bars. The background-colored map
561 shows the crustal thickness (a) and *Vp/Vs* (b). The earthquakes are indicated by white circles,
562 with strike-slip events shown in beach balls.

563

564 **Figure.8** Sketch map illustrating the layered deformation and the mismatch evolution between
565 GD and FJ. The regions of GD and FJ are shaded by different colors as the crusts in these areas
566 show distinct characteristics of the thickness and *Vp/Vs* ratio. The red arrows in the upper and

lower crust indicate the OPA and shearing-induced anisotropy due to the collision. The green dashed lines show the shearing zone between the upper and lower crusts. Red stars show devastating earthquakes located at the intersection of regional faults such as CNFZ and BFZ.

570 Figure.1

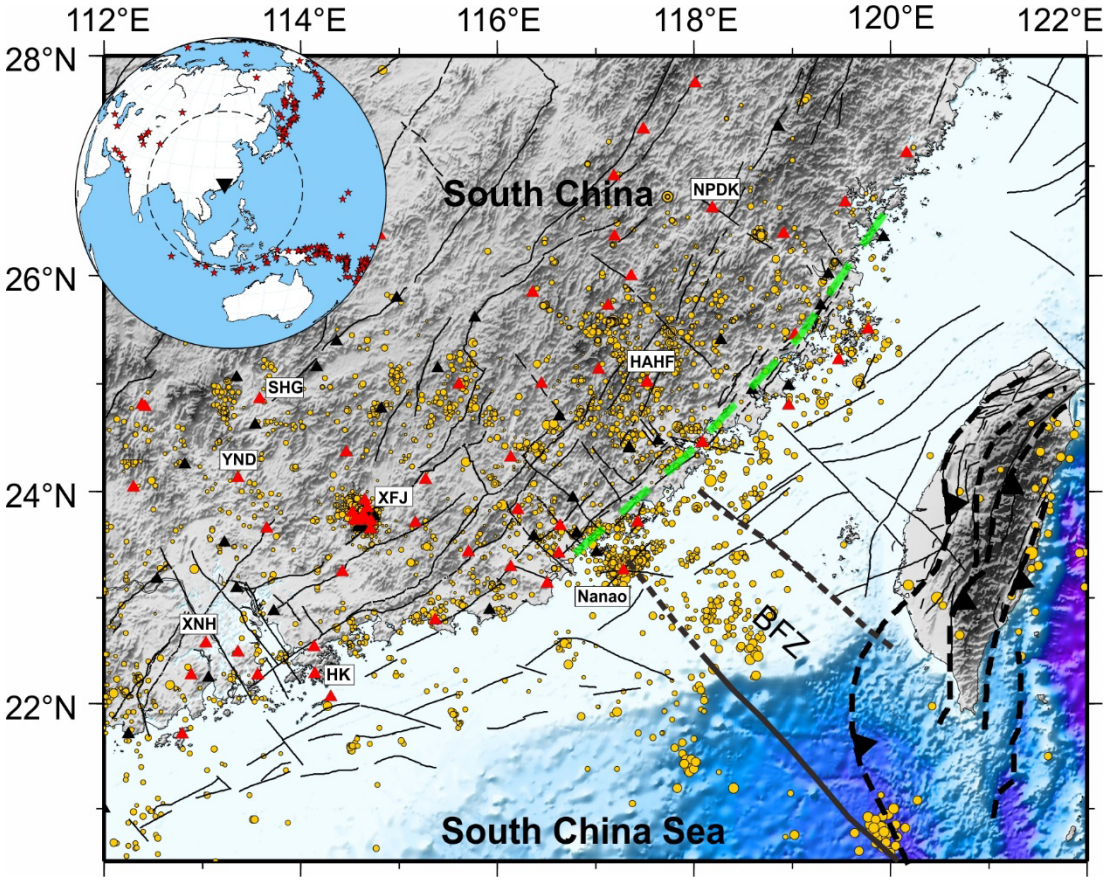

571

572 Figure.2

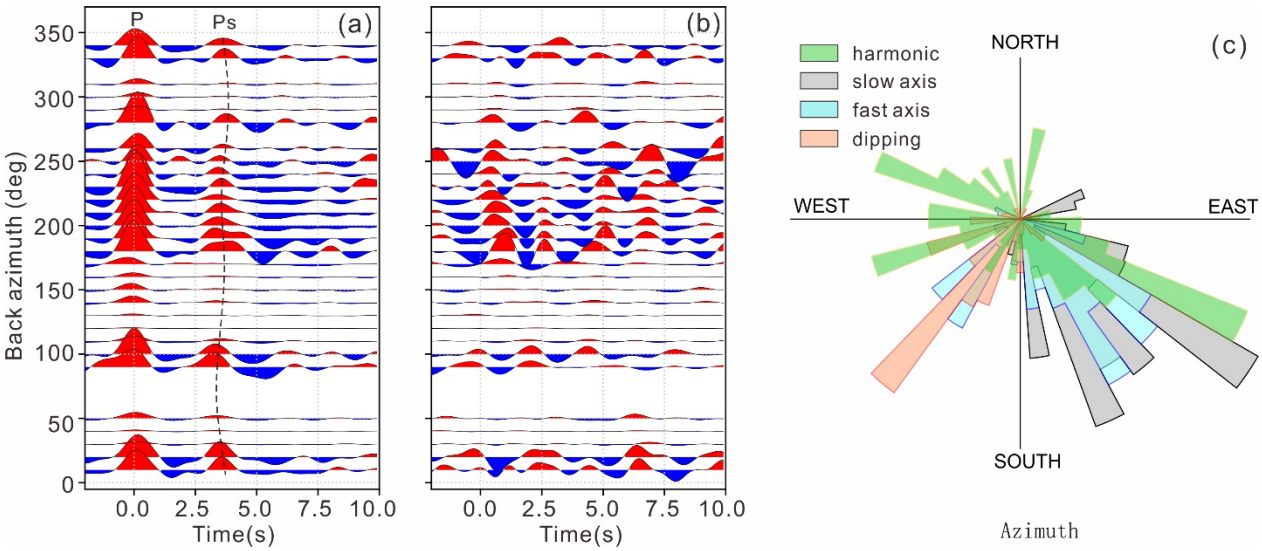

573

574 Figure.3

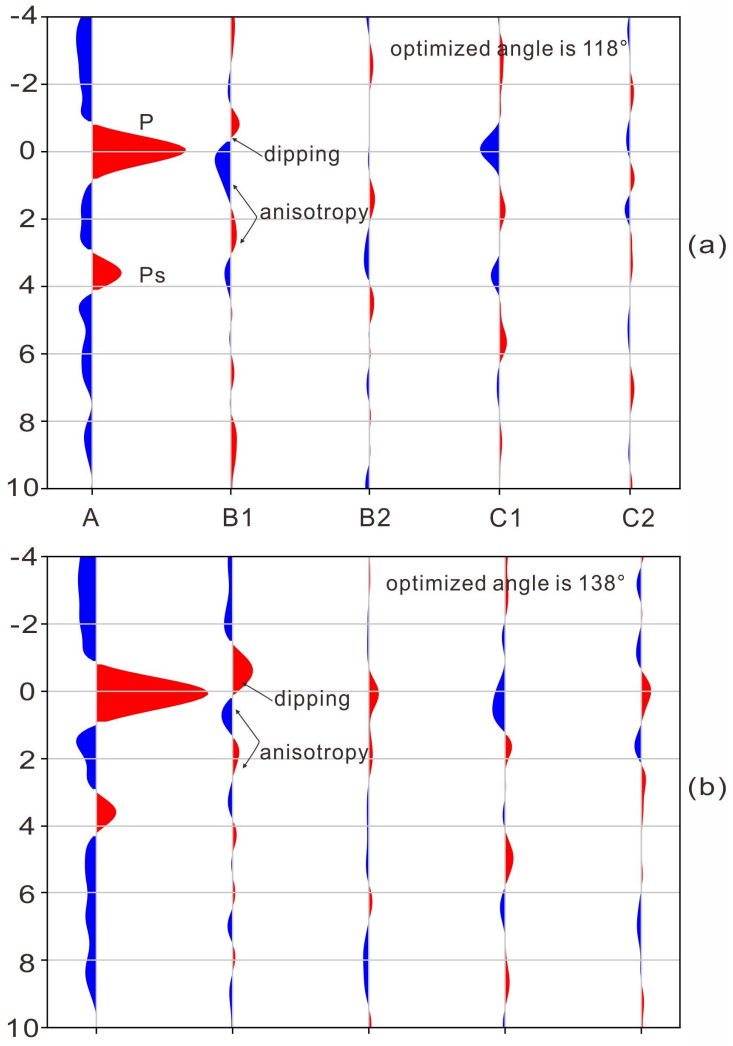

575

576 Figure.4

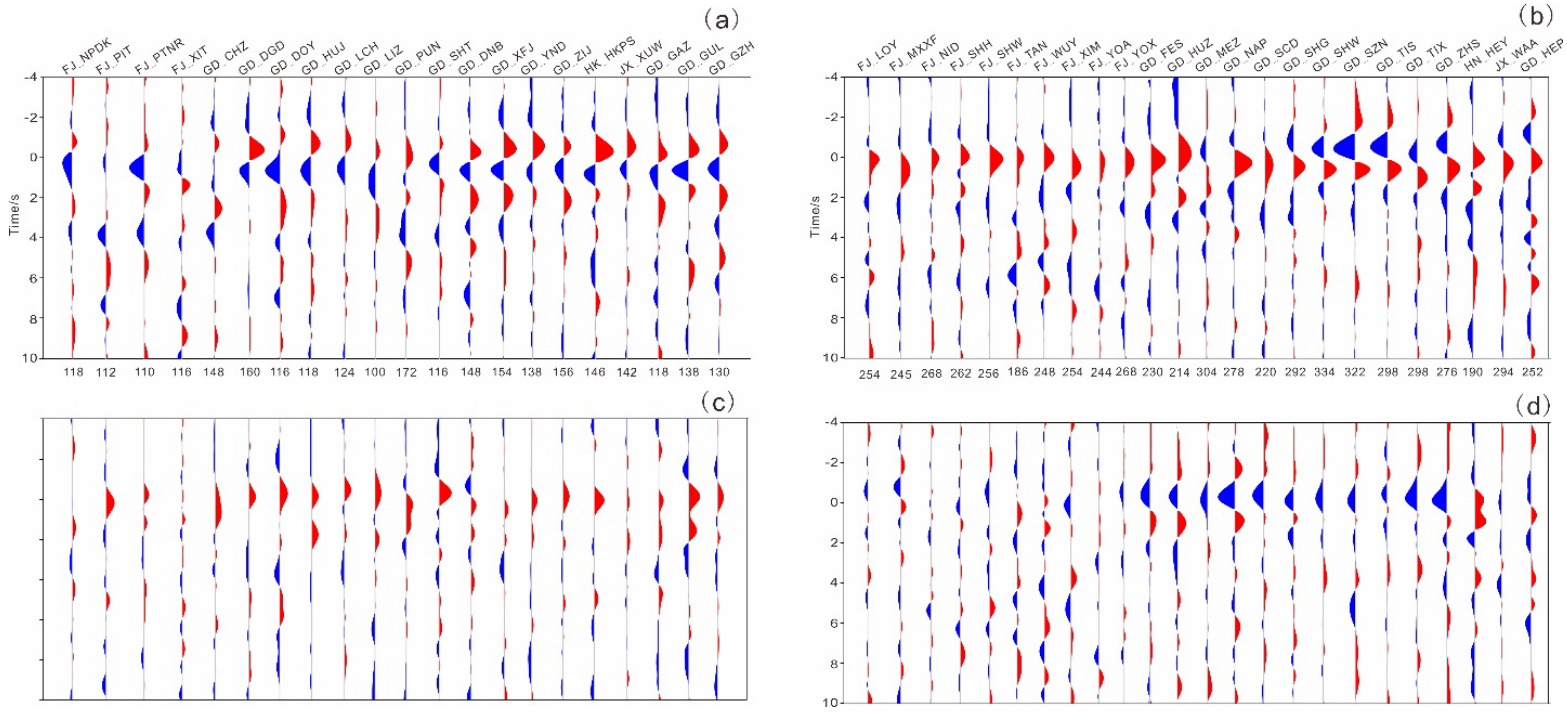

577

578 Figure.5

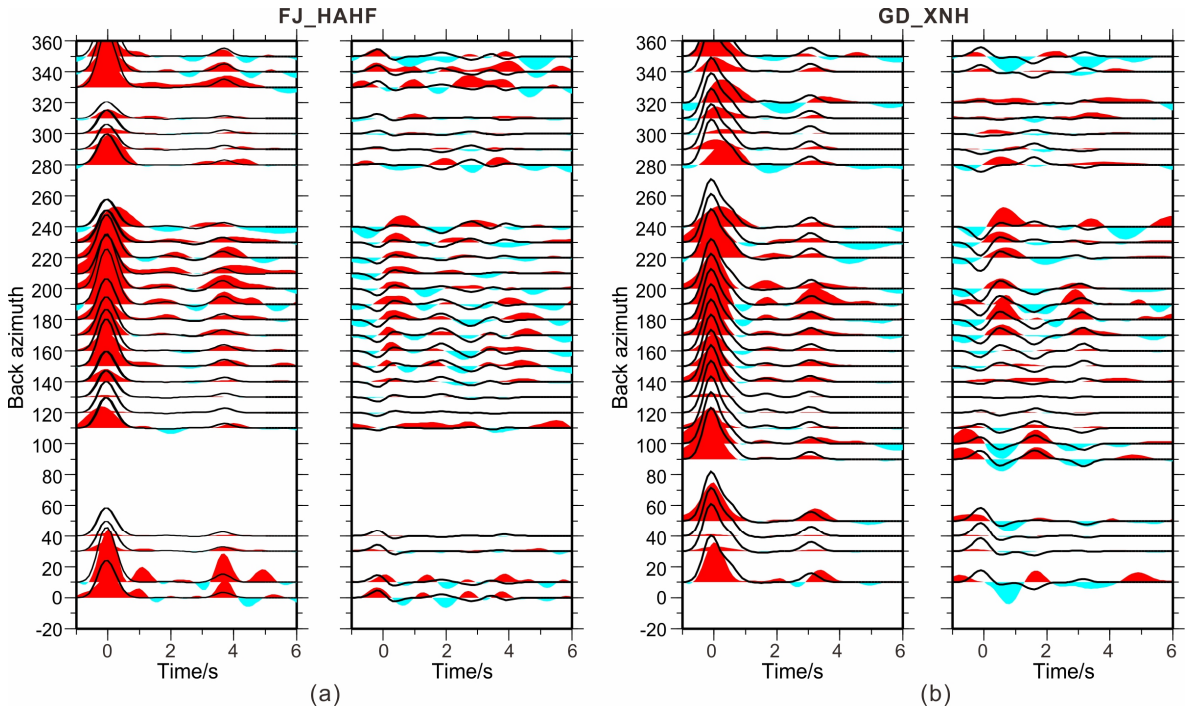

579

580 Figure.6

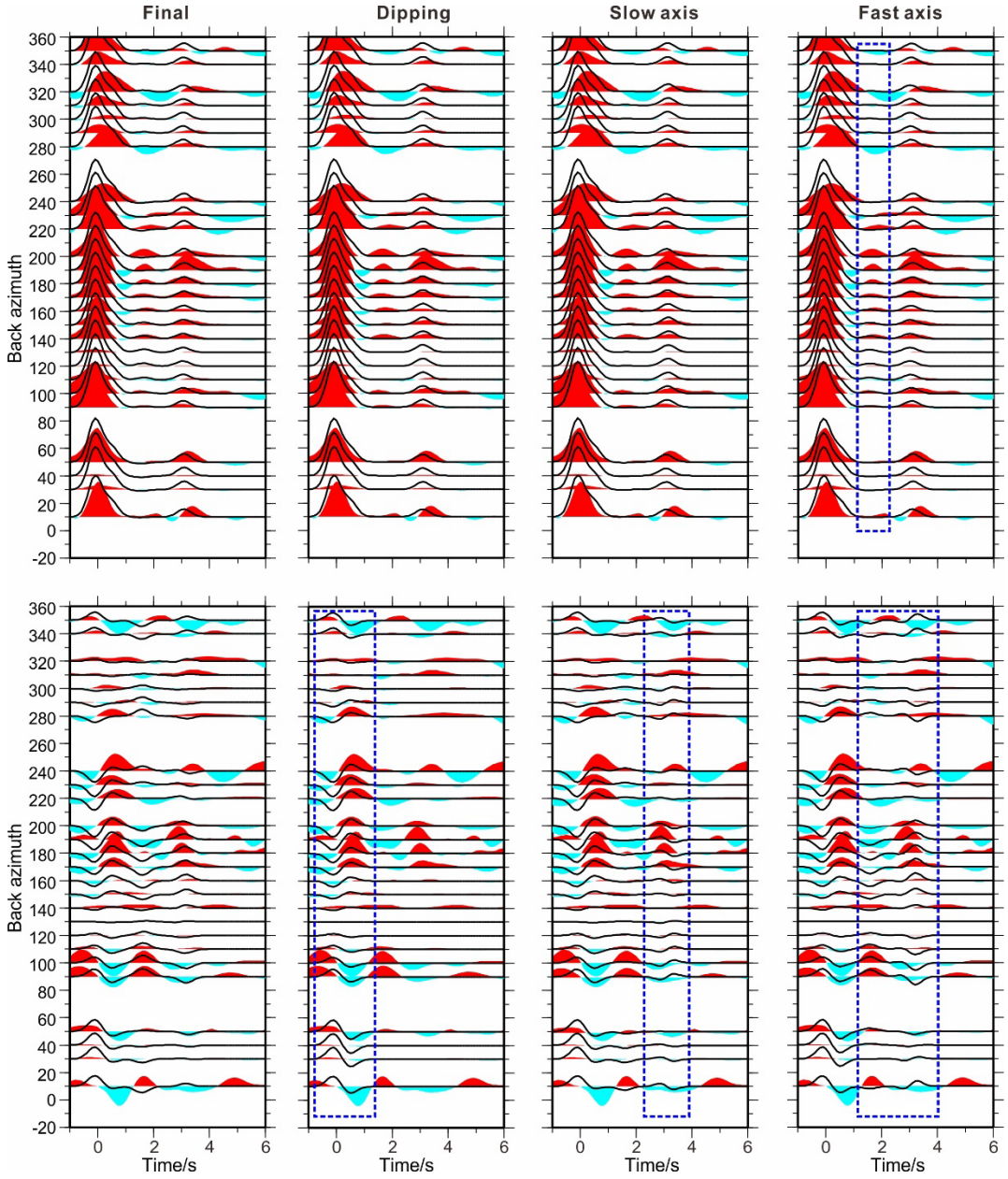

581

582 Figure.7

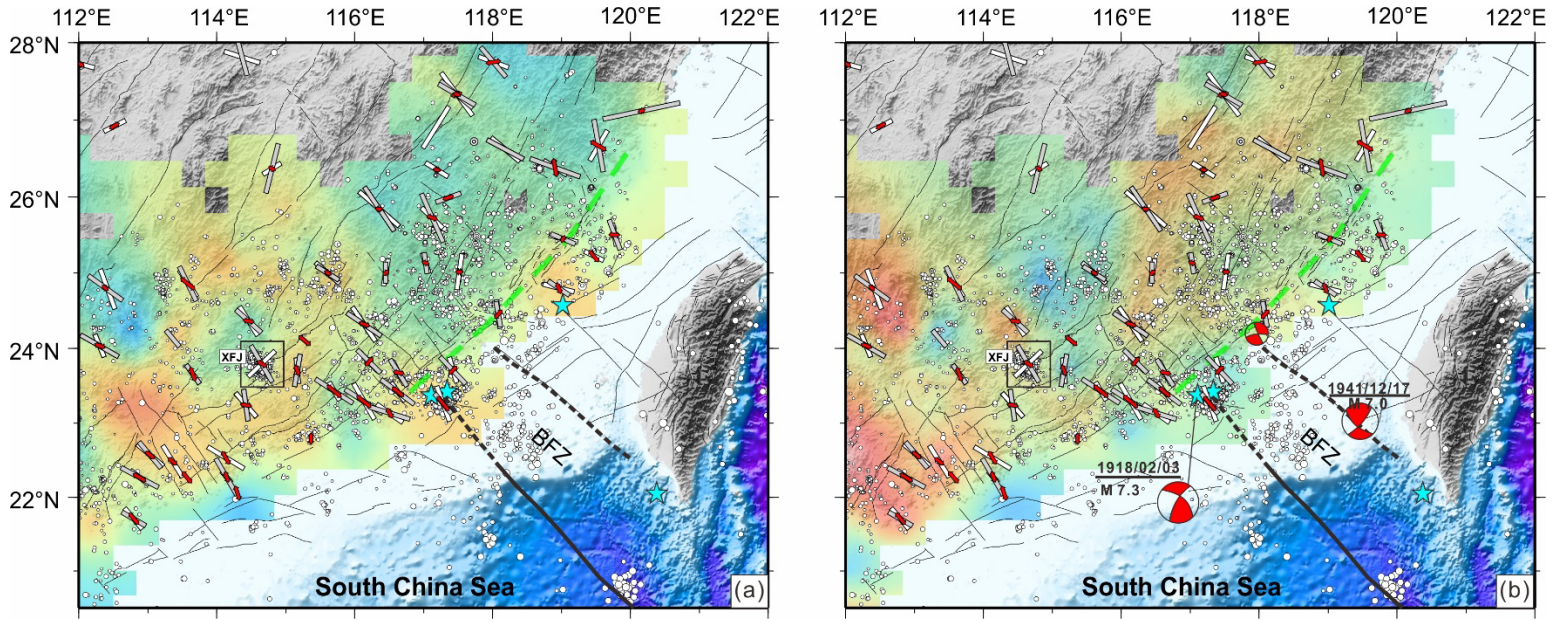

583

584 **Figure.8**

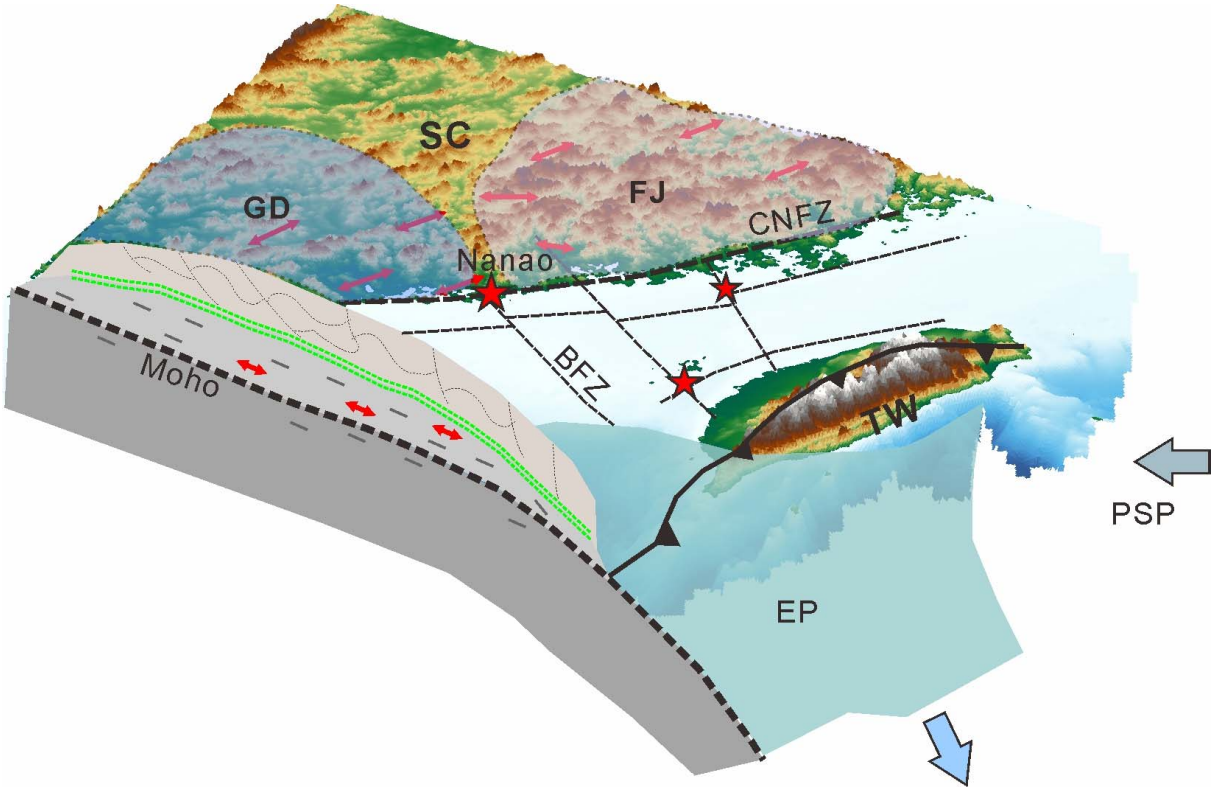

585

Figure 1.

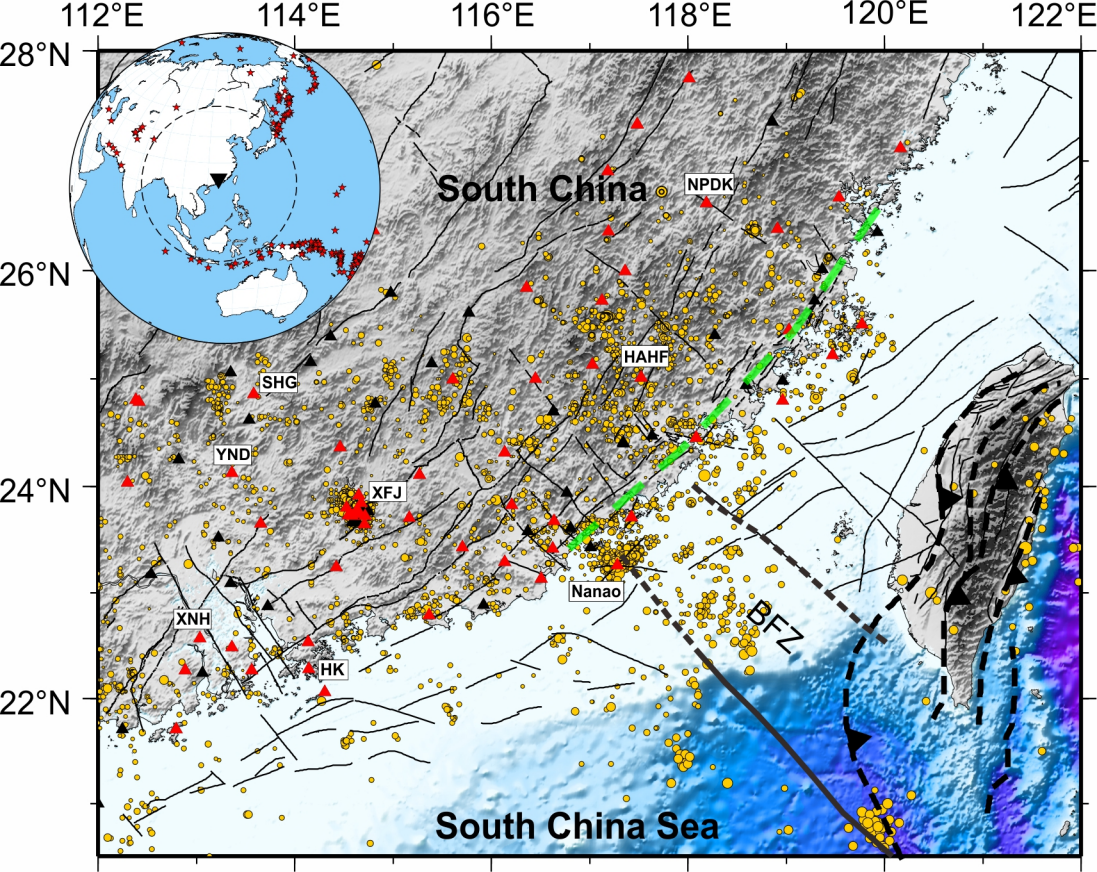
112°E
114°E
116°E
118°E
120°E
122°E
28°N
26°N
24°N
22°N
South China
NPDK
HAHF
SHC
YND
XFJ
Nanao
XNH
HK
BFZ
South China Sea

Figure 2.

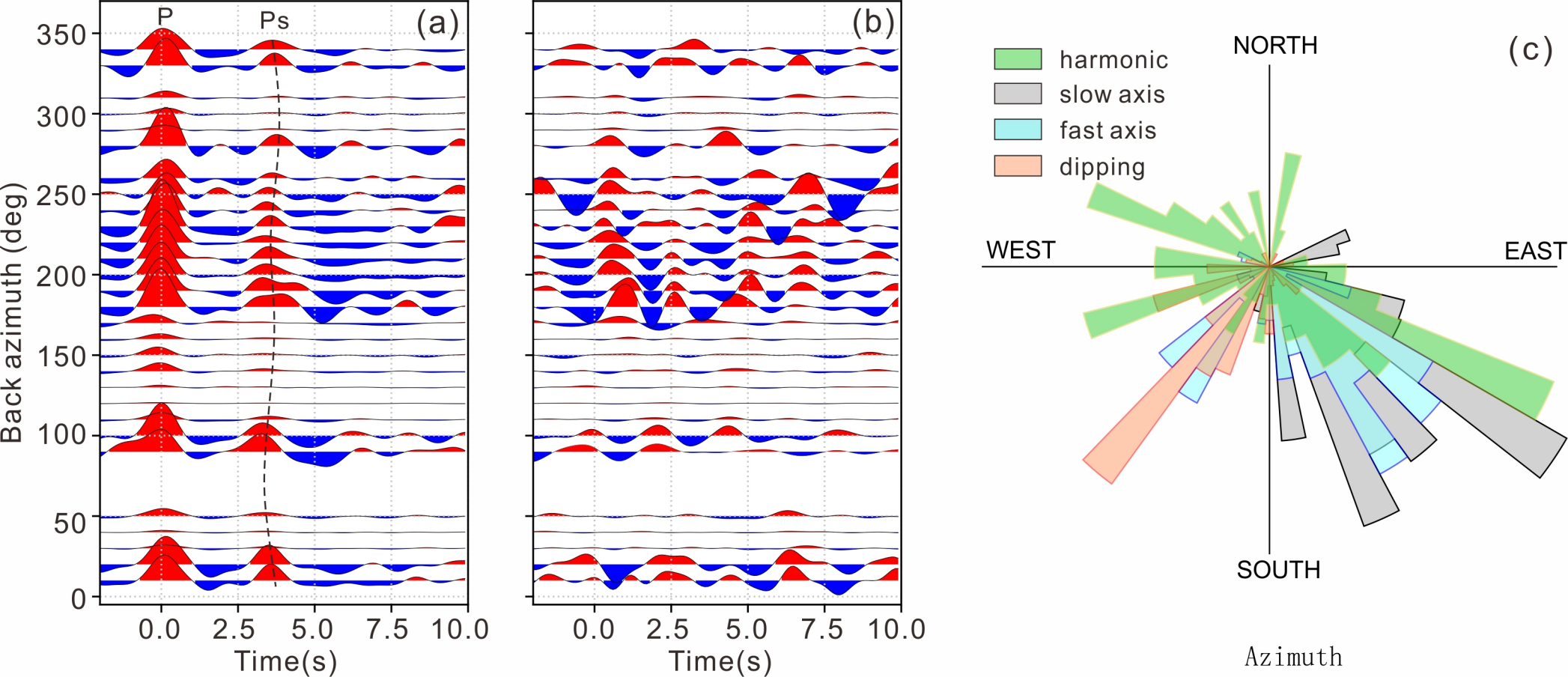
P
Ps
(a)
(b)
(c)
Back azimuth (deg)
350
300
250
200
150
100
50
0
0.0
2.5
5.0
7.5
10.0
Time(s)
harmonic
slow axis
fast axis
dipping
NORTH
WEST
EAST
SOUTH
Azimuth

Figure 3.

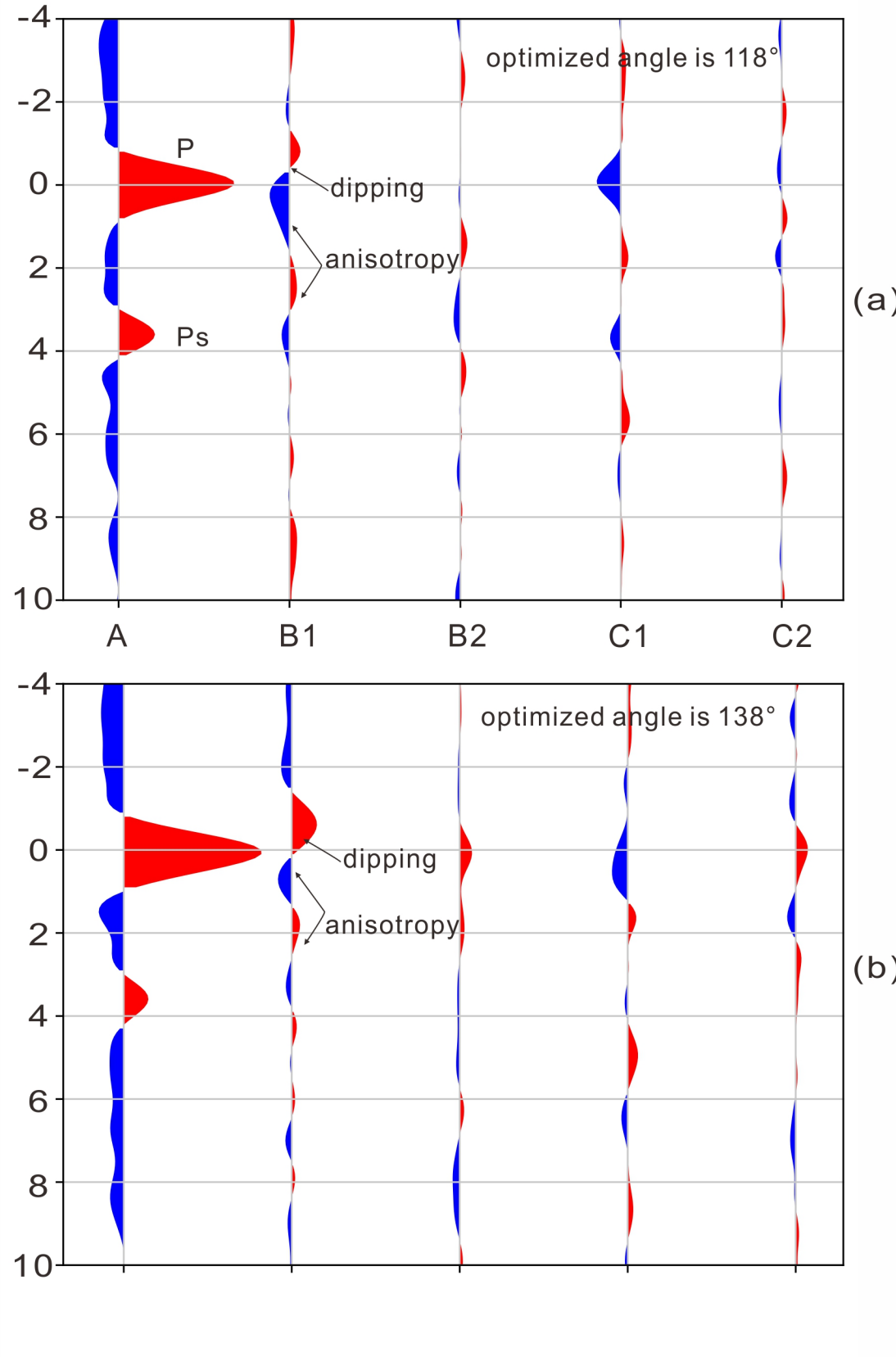
optimized angle is 118°
P
Ps
dipping
anisotropy
(a)
-4
-2
0
2
4
6
8
10
A
B1
B2
C1
C2
optimized angle is 138°
dipping
anisotropy
(b)

Figure 4.

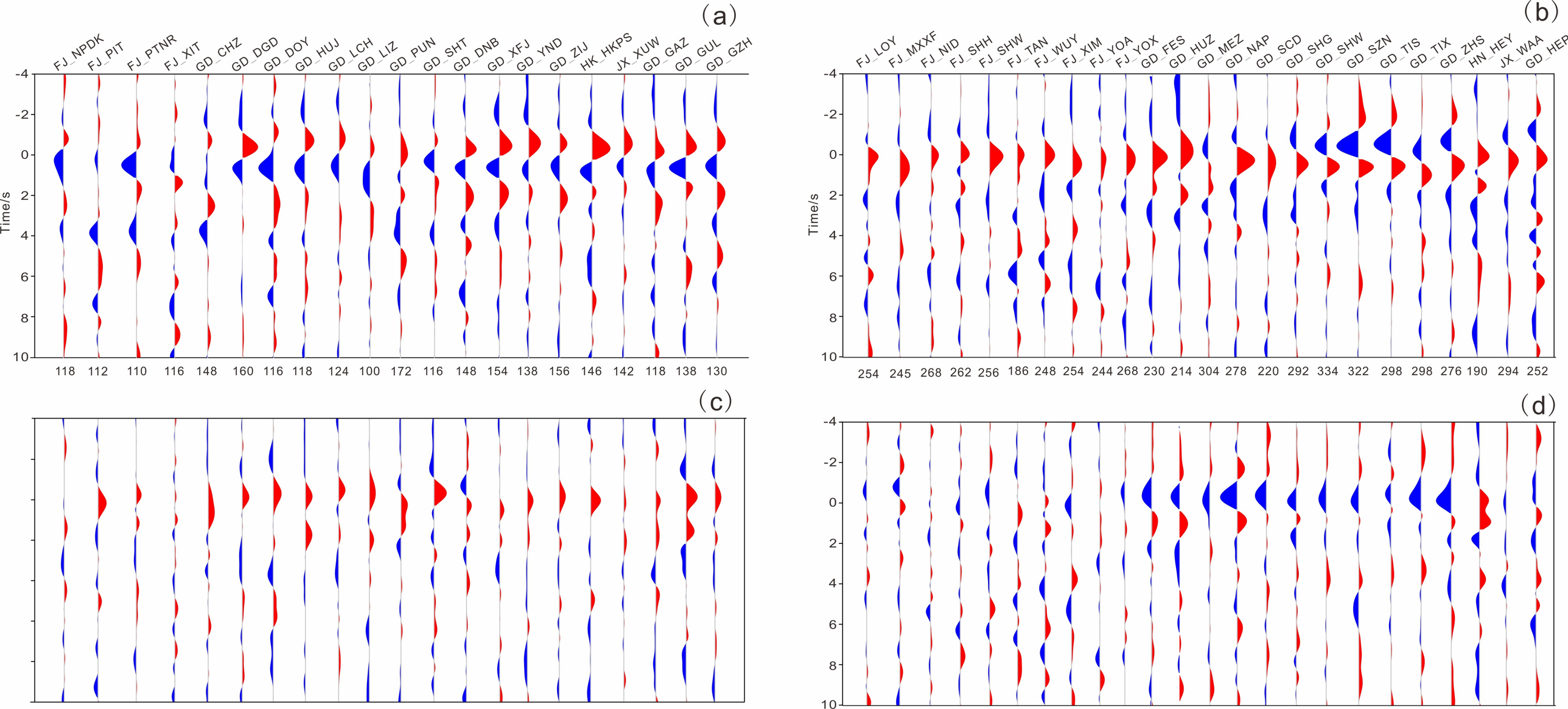
(a)
FJ_NPDK FJ_PIT FJ_PTNR FJ_XIT GD_CHZ GD_DGD GD_DOY GD_HUJ GD_LCH GD_LIZ GD_PUN GD_SHT GD_DNB GD_XFJ GD_YND GD_ZIJ HK_HKPS JX_XUW GD_GAZ GD_GUL GD_GZH
Time/s
-4 -2 0 2 4 6 8 10
118 112 110 116 148 160 116 118 124 100 172 116 148 154 138 156 146 142 118 138 130
(b)
FJ_LOY FJ_MXXF FJ_NID FJ_SHH FJ_SHW FJ_TAN FJ_WUY FJ_XIM FJ_YOA FJ_YOX GD_FES GD_HUZ GD_MEZ GD_NAP GD_SCD GD_SHG GD_SHW GD_SZN GD_TIS GD_TIX GD_ZHS HN_HEY JX_WAA GD_HEP
Time/s
-4 -2 0 2 4 6 8 10
254 245 268 262 256 186 248 254 244 268 230 214 304 278 220 292 334 322 298 298 276 190 294 252
(c)
(d)
-4 -2 0 2 4 6 8 10

Figure 5.

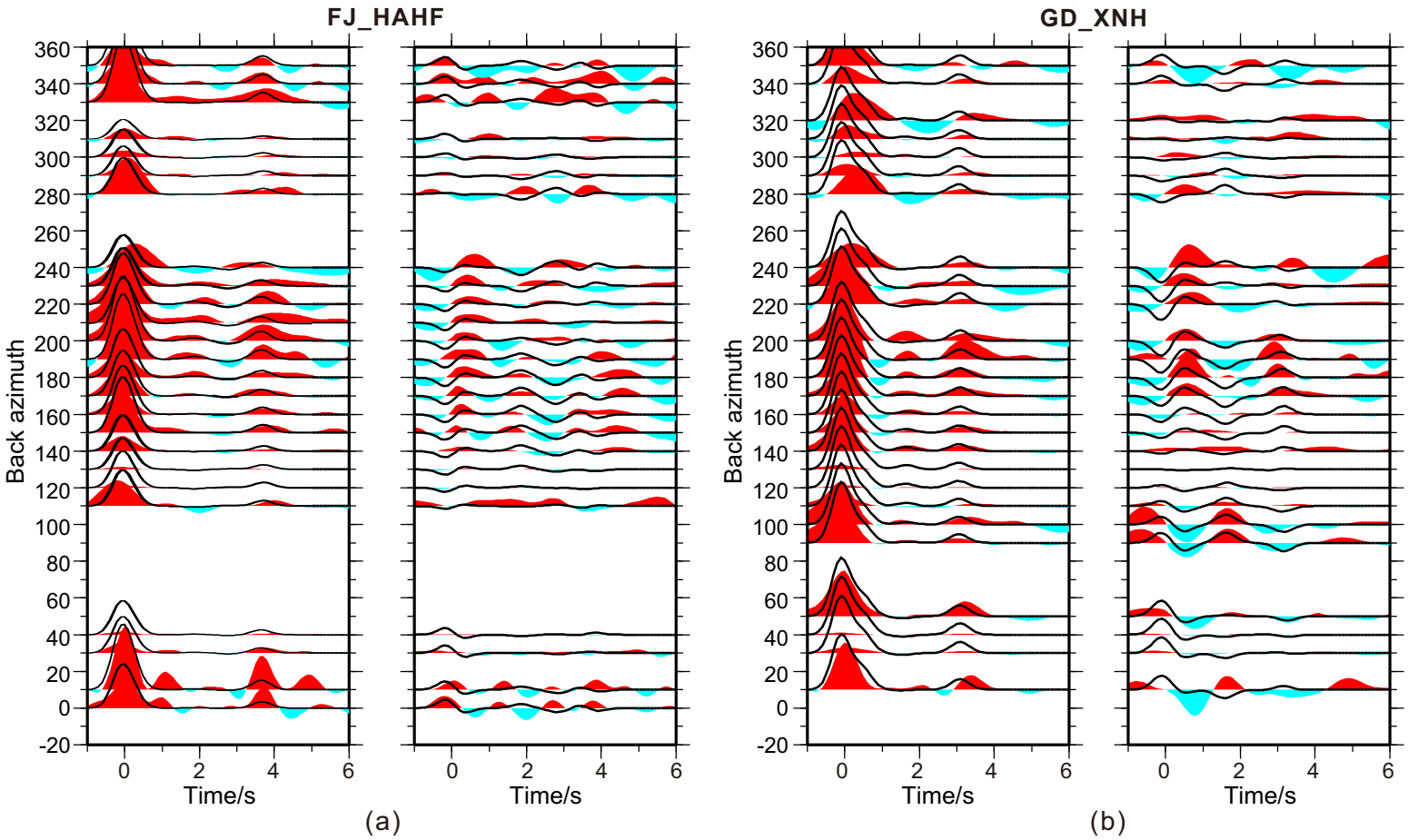
FJ_HAHF
GD_XNH
Back azimuth
360
340
320
300
280
260
240
220
200
180
160
140
120
100
80
60
40
20
0
-20
0
2
4
6
Time/s
(a)
(b)

Figure 6.

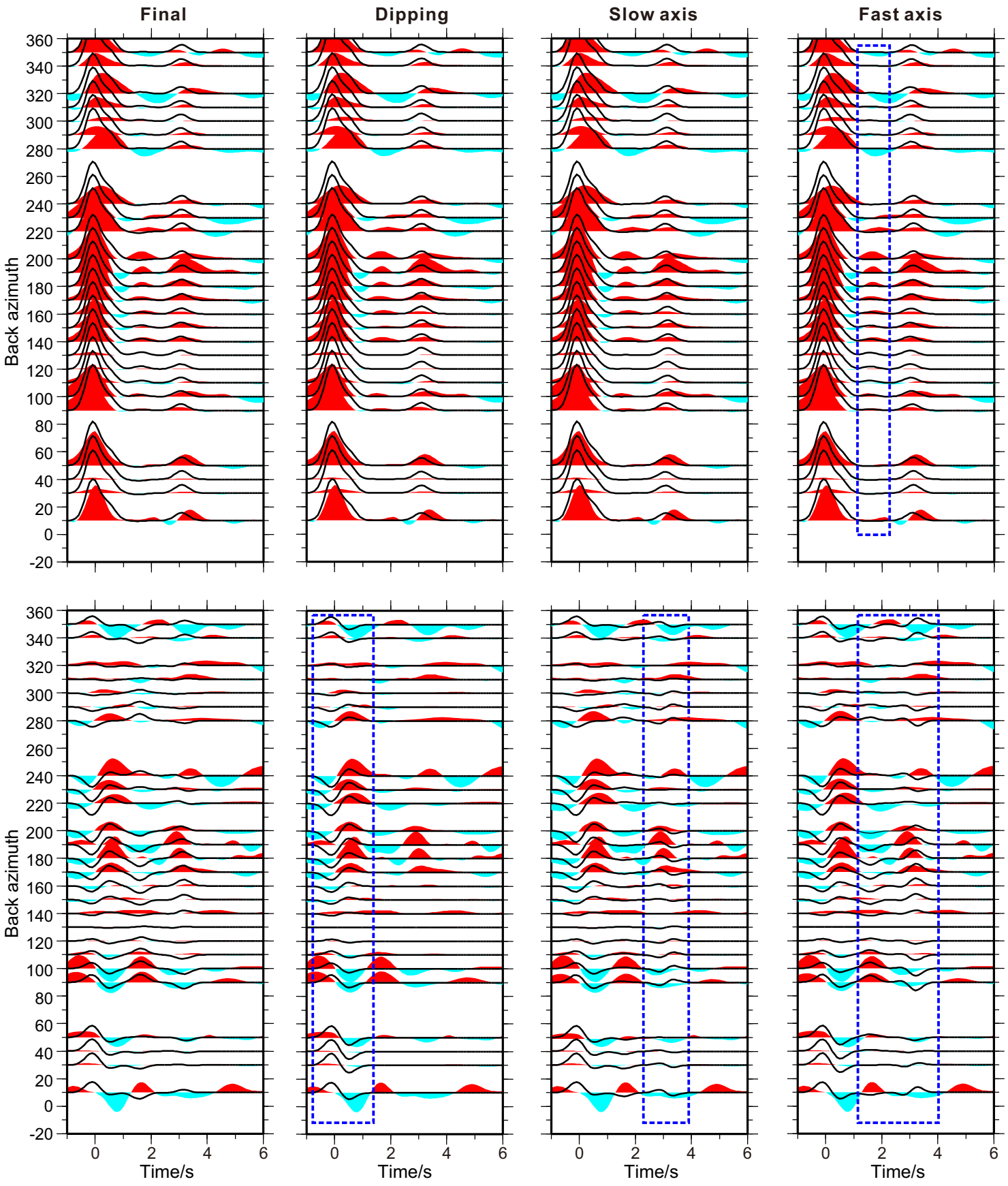
Final
Dipping
Slow axis
Fast axis
Back azimuth
360
340
320
300
280
260
240
220
200
180
160
140
120
100
80
60
40
20
0
-20
0
2
4
6
Time/s

Figure 7.

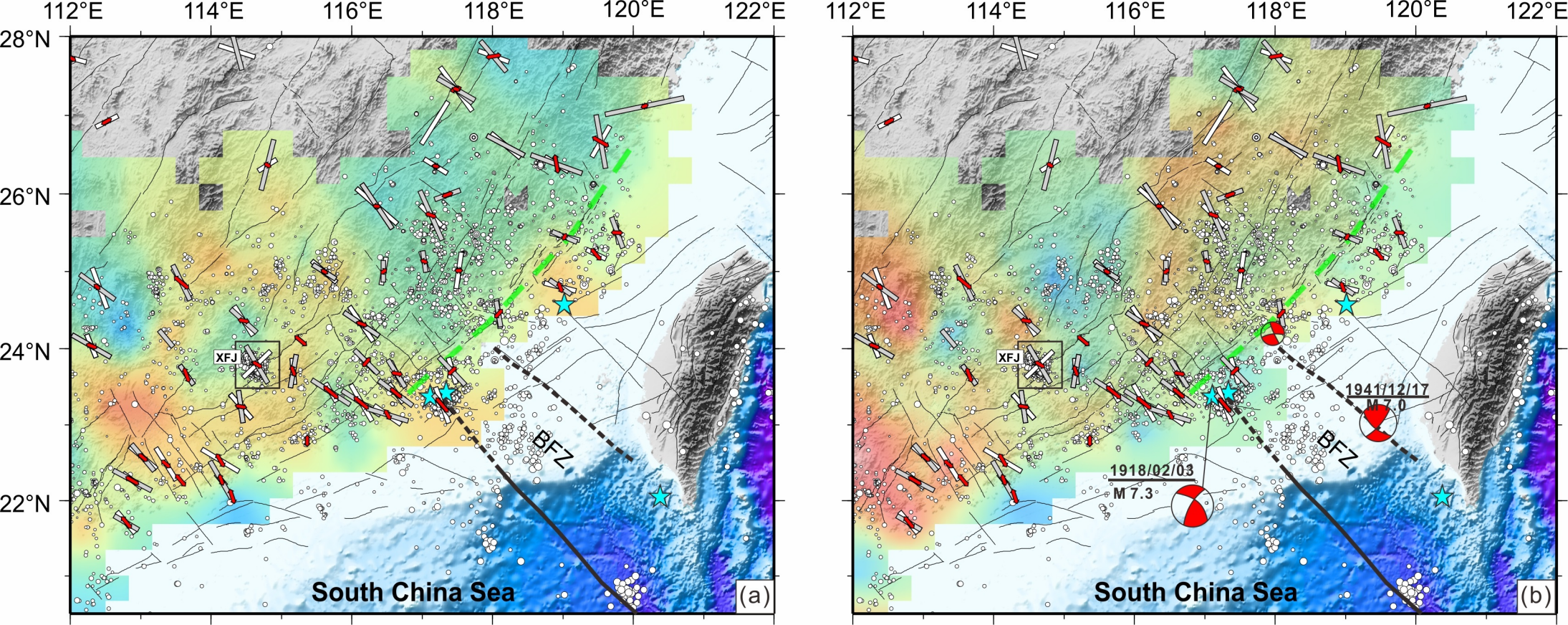
112°E
114°E
116°E
118°E
120°E
122°E
28°N
26°N
24°N
22°N
XFJ
BFZ
South China Sea
(a)
1941/12/17
M 7.0
1918/02/03
M 7.3
(b)

Figure 8.

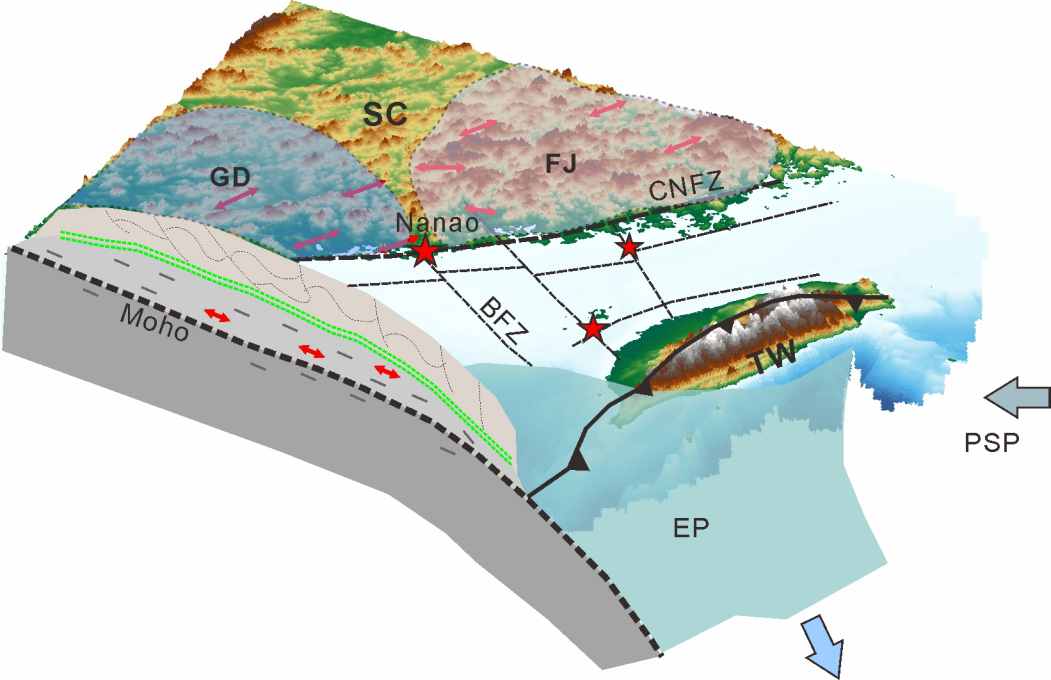
SC
GD
FJ
CNFZ
Nanao
BFZ
Moho
TW
PSP
EP